



# The First Bird's-eye View of a Gravitationally Unstable Accretion Disk in High-mass Star Formation

Kazuhiro Motogi<sup>1</sup>, Tomoya Hirota<sup>2,3</sup> , Masahiro N. Machida<sup>4</sup> , Yoshinori Yonekura<sup>5</sup> , Mareki Honma<sup>3,6</sup> ,  
Shigehisa Takakuwa<sup>7</sup>, and Satoki Matsushita<sup>8</sup>

<sup>1</sup> Graduate School of Sciences and Technology for Innovation, Yamaguchi University, Yoshida 1677-1, Yamaguchi 753-8512, Japan; [kmotogi@yamaguchi-u.ac.jp](mailto:kmotogi@yamaguchi-u.ac.jp)

<sup>2</sup> Mizusawa VLBI Observatory, National Astronomical Observatory of Japan, Osawa 2-21-1, Mitaka, Tokyo 181-8588, Japan

<sup>3</sup> Department of Astronomical Sciences, SOKENDAI (The Graduate University for Advanced Studies), Osawa 2-21-1, Mitaka, Tokyo 181-8588, Japan

<sup>4</sup> Department of Earth and Planetary Sciences, Faculty of Sciences, Kyushu University, Motooka 744, Nishi-ku, Fukuoka-shi, Fukuoka 819-0395, Japan

<sup>5</sup> Center for Astronomy, Ibaraki University, 2-1-1 Bunkyo, Mito, Ibaraki 310-8512, Japan

<sup>6</sup> Mizusawa VLBI Observatory, National Astronomical Observatory of Japan, Hoshigaoka 2-12, Mizusawa, Oshu, Iwate 023-0861, Japan

<sup>7</sup> Department of Physics and Astronomy, Graduate School of Science and Engineering, Kagoshima University, 1-21-35 Korimoto, Kagoshima, Kagoshima 890-0065, Japan

<sup>8</sup> Academia Sinica, Institute of Astronomy and Astrophysics (ASIAA), P.O. Box 23-141, Taipei, 10617, Taiwan

Received 2019 March 30; revised 2019 May 10; accepted 2019 May 12; published 2019 May 29

## Abstract

We report on the first bird's-eye view of the innermost accretion disk around the high-mass protostellar object G353.273+0.641, taken by Atacama Large Millimeter/submillimeter Array long baselines. The disk traced by dust continuum emission has a radius of 250 au, surrounded by the infalling rotating envelope traced by thermal CH<sub>3</sub>OH lines. This disk radius is consistent with the centrifugal radius estimated from the specific angular momentum in the envelope. The lower-limit envelope mass is  $\sim 5\text{--}7 M_{\odot}$  and accretion rate onto the stellar surface is  $3 \times 10^{-3} M_{\odot} \text{ yr}^{-1}$  or higher. The expected stellar age is well younger than  $10^4$  yr, indicating that the host object is one of the youngest high-mass objects at present. The disk mass is  $2\text{--}7 M_{\odot}$ , depending on the dust opacity index. The estimated Toomre's  $Q$  parameter is typically 1–2 and can reach 0.4 at the minimum. These  $Q$  values clearly satisfy the classical criteria for gravitational instability, and are consistent with recent numerical studies. Observed asymmetric and clumpy structures could trace a spiral arm and/or disk fragmentation. We found that 70% of the angular momentum in the accretion flow could be removed via the gravitational torque in the disk. Our study has indicated that the dynamical nature of a self-gravitating disk could dominate the early phase of high-mass star formation. This is remarkably consistent with the early evolutionary scenario of a low-mass protostar.

**Key words:** ISM: individual objects (G353.273+0.641) – ISM: molecules – radio continuum: ISM – stars: formation

## 1. Introduction

In the last two decades, 10 or more accretion disk candidates, which play critical roles in low-mass star formation, have been found for high-mass stars (Cesaroni et al. 2006; Beltrán & de Wit 2016). The final stellar mass and evolutionary pathway of high-mass protostars should be determined by physical processes inside a disk (e.g., Hosokawa et al. 2010). However, almost all of the known resolved disks around high-mass stars are nearly edge-on to the disk; this is easy to detect due to the maximized rotating motion along the line of sight (LOS). Consequently, no one has ever directly seen the innermost region of a disk. This Letter reports on the first Atacama Large Millimeter/submillimeter Array (ALMA) long baseline imaging toward the nearly face-on high-mass protostellar object G353.273+0.641 (hereafter G353).

G353 is a relatively nearby high-mass object ( $\sim 1.7$  kpc) without any compact H II region (Motogi et al. 2016, 2017). The stellar mass is  $\sim 10 M_{\odot}$  and is still in the main accretion phase, as suggested by active outflow activities (Motogi et al. 2013, 2016). Previous studies have shown that G353 has an almost face-on accretion system, where the disk rotational axis is inclined  $\sim 8^{\circ}$  from the LOS (Motogi et al. 2016, 2017). Therefore, G353 is the best target for direct imaging of any radial structures in the disk, minimizing a self-absorption effect by an optically thick dusty system as reported by recent ALMA observations (e.g., Beuther et al. 2017). In particular, Motogi

et al. (2017) observed 6.7 GHz CH<sub>3</sub>OH masers and found the three-dimensional infalling streams from 100 to 15 au. They discussed possibilities of very small initial angular momentum and/or significant angular momentum transfer outside 100 au in radius. This work directly resolved  $10^2\text{--}10^3$  au scale and examined these possibilities.

## 2. Observation and Reduction

We performed high-resolution ( $\sim 85$  au) imaging of the dust continuum and several CH<sub>3</sub>OH lines at 150 GHz in ALMA Cycle 4. Forty-five antennas were used in the long baseline configuration (up to  $\sim 12$  km). The total on-source time was 5 minutes. We observed four 1.875 GHz wide sub-bands centered on 142.692, 144.571, 154.613, and 156.491 GHz (ALMA band 4). Only the sub-band at 156.491 GHz, which had the highest spectral resolution of 488.281 kHz ( $0.94 \text{ km s}^{-1}$ ), was used for the line analysis. We integrated all four sub-bands for the dust continuum analysis after the line subtraction.

The data were calibrated in the standard manner of ALMA by using the CASA software package version 5.3.0 (McMullin et al. 2007). No self-calibration was performed. The uncertainties are dominated by the error of the absolute flux scaling using the quasar J1733–1304 ( $\sim 10\%$ ). Therefore we adopt 10% error for all the fluxes and/or brightness temperature ( $T_{\text{B}}$ ) in this Letter.

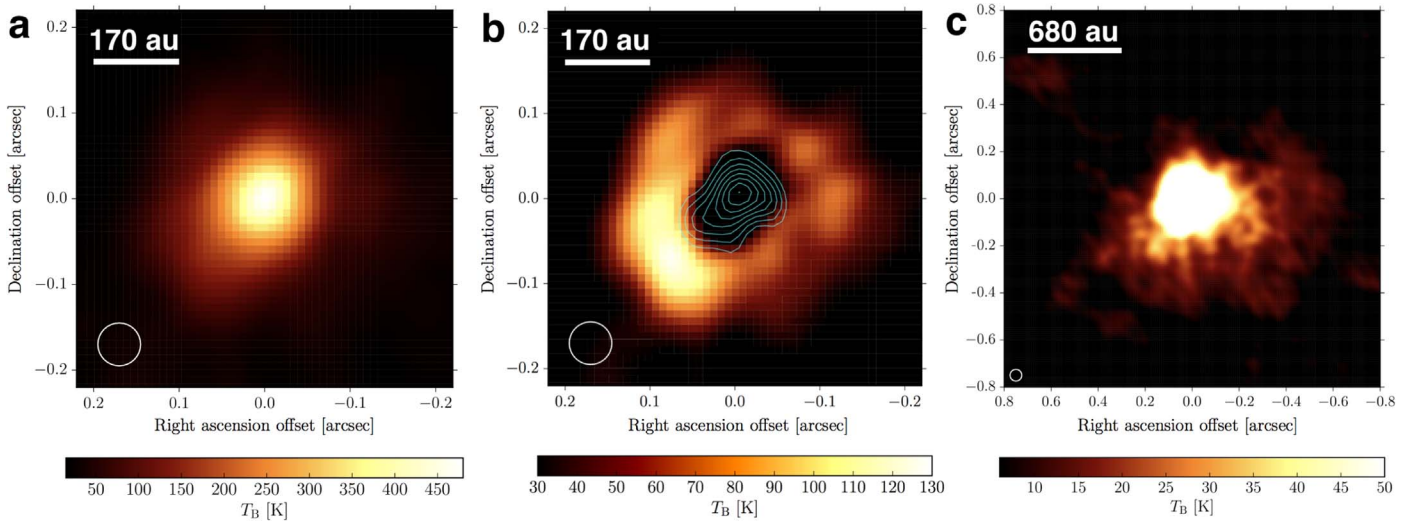


**Figure 1.** (a) Original dust continuum image near the center. The white circle represents the synthesized beam for continuum. (b) Residual image after the subtraction of the compact emission. Contours show the continuum at 45 GHz in Motogi et al. (2017), which are every 25 K starting from 100 K ( $5\sigma$ ). (c) The entire distribution of dust continuum emission. The color scale is artificially saturated at 50 K ( $18.5\sigma$ ), in order to highlight diffuse extended emission.

**Table 1**  
The Elliptical Gaussian Parameters of the Compact Component

Frequency (GHz)	Major Axis (au)	Minor Axis (au)	Position Angle (degree)	Total Flux (mJy)	Peak $T_B$ (K)
45 <sup>a</sup>	$209 \pm 7$	$124 \pm 14$	$143 \pm 5$	$3.5 \pm 0.1$	278
150	$177 \pm 0.3$	$136 \pm 0.2$	$149 \pm 0.3$	$72.5 \pm 0.2$	480

**Note.**

<sup>a</sup> The data at 45 GHz is from Motogi et al. (2017).

Original synthesized beams were  $0''.085 \times 0''.050$  ( $145 \times 85 \text{ au}^2$ ) and  $0''.099 \times 0''.075$  ( $168 \times 128 \text{ au}^2$ ) for the continuum and  $\text{CH}_3\text{OH}$  lines, respectively. The beam position angle for the continuum and lines were  $48^\circ.7$  and  $51^\circ.4$  (east of north), respectively. For fair comparison between new 150 GHz data and previous J-VLA 45 GHz data, the obtained continuum image was finally reconstructed by using the circular beam of  $0''.050 \times 0''.050$  as in the previous study (Motogi et al. 2017), where all the clean components were reconvolved by the circular beam in the deconvolution process. The final image noise level ( $1\sigma$ ) is 2.7 K for the continuum, and 7.5 K for line emission after the line stacking analysis (see below). The continuum peak position was  $17^{\text{h}}26^{\text{m}}01^{\text{s}}58798$ ,  $-34^\circ15'14''.9175$  (J2000.0). We used this position as the coordinate origin of all the spatial maps in this Letter.

### 3. Results and Discussions

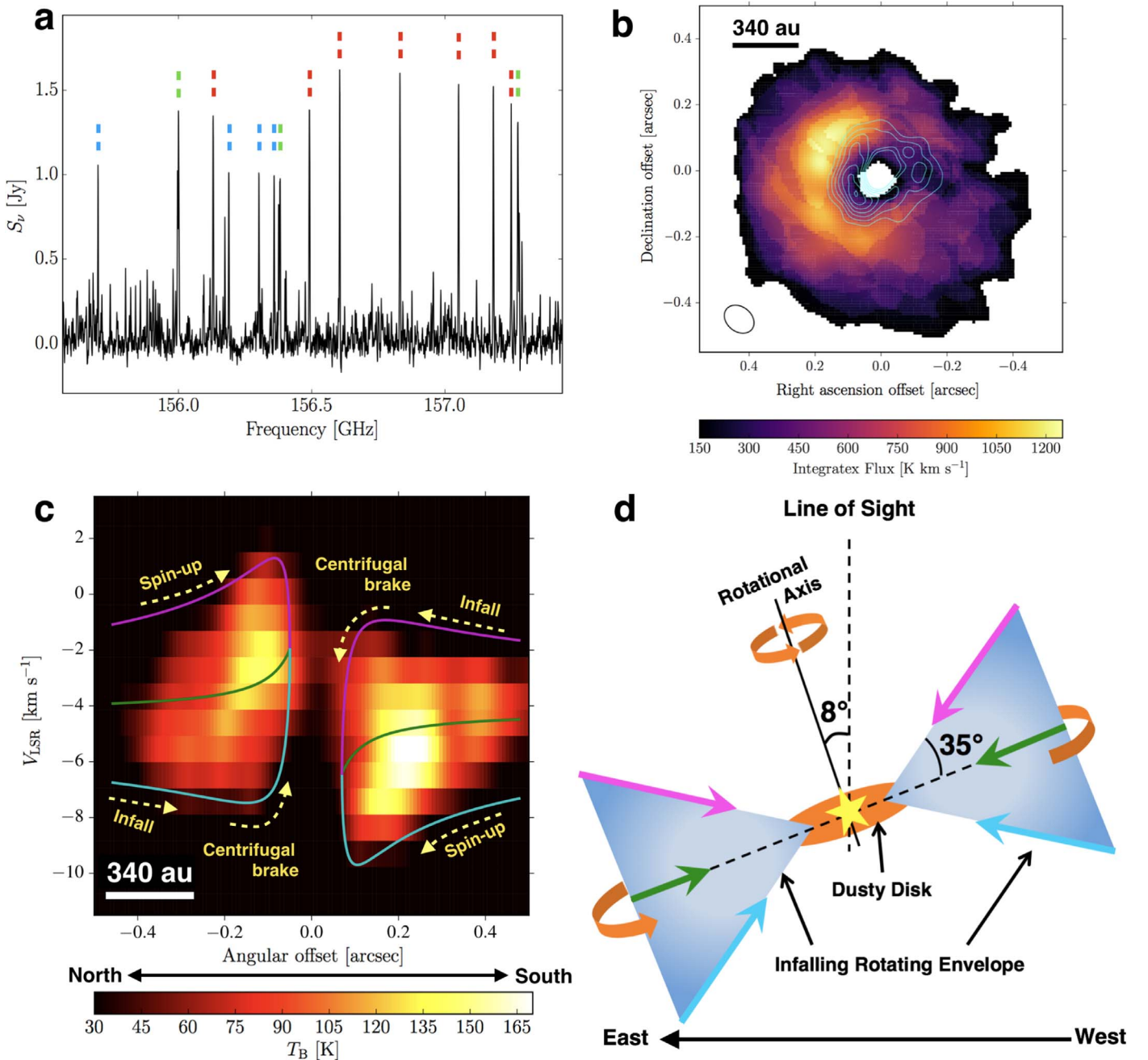
#### 3.1. Dust Continuum

Figure 1(a) shows the dust continuum image of the accretion disk that consists of the compact central emission and resolved structure. The latter was highlighted in Figure 1(b), where the former compact emission was subtracted by elliptical Gaussian fitting (Appendix A). The compact emission has an averaged diameter of  $\sim 160$  au (Table 1). The peak  $T_B$  is 480 K. The resolved structure is almost “ring-like” with the outer radius of 250 au. There are an arc-like elongated feature in the east and several clumpy features in the west. The peak  $T_B$  in the east side (up to 126 K) is 2–3 times brighter compared to other, less bright parts. This asymmetry would reflect the contrast of the

surface density rather than the asymmetric temperature profile, as the disk temperature should be basically dominated by stellar radiation in this small scale. It should be noted that, if the disk actually has a non-axisymmetric structure such as spiral arms, the dynamical heating effect can cause a deviation from the axisymmetric temperature profile. Although few limited studies observed the innermost accretion system in high-mass star formation (Cesaroni et al. 2014; Beuther et al. 2017; Hirota et al. 2017), this is the first completely resolved view of such a compact non-axisymmetric structure inside a disk.

The compact emission is consistent with the continuum emission at 45 GHz previously reported in Motogi et al. (2017) as shown in Figure 1(b) and Table 1, indicating that we could successfully subtract the hot and compact emission in the innermost region. The spectral index is  $2.5 \pm 0.2$  between 45 and 150 GHz, considering the flux uncertainty of 10%. The optical depth, averaged surface density ( $N_{\text{H}_2}$ ), and total mass of the compact emission are  $2.0_{-0.9}^{+1.4}$ ,  $8.2_{-3.8}^{+5.7} \times 10^{25} \text{ cm}^{-2}$  and  $0.8_{-0.4}^{+0.5} M_\odot$ , respectively (Appendix A). On the other hand, the optical depth in the resolved structure was determined as  $0.68_{-0.30}^{+0.36}$  at the eastern peak and  $0.31 \pm 0.12$  on average, which corresponds to the surface densities of  $2.8_{-1.2}^{+1.5} \times 10^{25} \text{ cm}^{-2}$  and  $1.3 \pm 0.5 \times 10^{25} \text{ cm}^{-2}$ , respectively. The total mass of the dusty accretion system is  $1.9_{-0.8}^{+1.0} M_\odot$ , including the compact component. Here we adopted the dust mass opacity of  $0.59 \text{ cm}^2 \text{ g}^{-1}$  at 150 GHz and the gas-to-dust ratio of 100 (Appendix A).

Figure 1(c) shows the entire continuum emission in a further large-scale envelope ( $\sim 700$  au in radius). The integrated flux density is 316 mJy ( $>3\sigma$  level), including 140 mJy from the



**Figure 2.** (a) Spectrum of the detected  $\text{CH}_3\text{OH}$  lines. We marked several strong emission by dashed lines. Red and blue dashed lines indicate  $\text{CH}_3\text{OH}$  and  $^{13}\text{CH}_3\text{OH}$  transitions, respectively. Green dashed lines indicate blended lines, where multiple  $\text{CH}_3\text{OH}$  or  $^{13}\text{CH}_3\text{OH}$  transitions are blended. (b) Integrated flux map of the  $\text{CH}_3\text{OH}$  emission (Appendix B). Contours show the dust emission in Figure 1(b) at every 15 K starting from 40 K ( $15\sigma$ ). The black ellipse represents the synthesized beam for line emissions. (c)  $PV$  diagram of the stacked  $\text{CH}_3\text{OH}$  emission along  $x = 0''$  in Figure 2(b).  $V_{\text{LSR}}$  denotes the LOS velocity with respect to the local standard of rest. The origin of the angular offset is the continuum peak position. Magenta, cyan, and green lines indicate the LOS velocities on the near/far side and midplane calculated by the envelope model as shown in Figure 2(d), respectively (Appendix B). (d) Schematic view of the system seen edge-on. Magenta, cyan, and green arrows indicate infalling directions, corresponding to the velocity models in Figure 2(c).

compact emission within 250 au. The mass outside of 250 au is  $\sim 5 M_\odot$ , which is estimated by the graybody emission adopting the same dust parameters and the averaged temperature of  $\sim 100$  K that is deduced from line emissions (see the next subsection). The total mass of the entire system within 700 au radius is  $7 M_\odot$ . The uncertainty of these mass estimations originates primarily from the uncertainty of the dust parameter. This will be discussed later.

### 3.2. $\text{CH}_3\text{OH}$ Lines

We have detected seven  $\text{CH}_3\text{OH}$  lines (Figure 2(a) and Table 2). Figure 2(b) presents the integrated intensity map of the molecular envelope that has a comparable scale with that of the entire dust emission. Here, we stacked three  $\text{CH}_3\text{OH}$  lines, with the upper-state rotational energy higher than 70 K (Appendix B). It should be noted that all of the detected lines are thought to be not maser but thermal emission, because of the extended structure and moderate brightness. The envelope

**Table 2**  
Detected CH<sub>3</sub>OH and <sup>13</sup>CH<sub>3</sub>OH Lines

Transition <sup>a</sup> $J_K$	Frequency (GHz)	Upper-state Energy (K)	Ortho/Para <sup>b</sup>	Category <sup>c</sup>
Stacked CH <sub>3</sub> OH Lines				
2 <sub>1</sub> – 3 <sub>0</sub>	156.60235	21.4	A	Cold
6 <sub>2</sub> – 7 <sub>1</sub>	156.12770	86.5	A	Hot
8 <sub>0</sub> – 8 <sub>-1</sub>	156.48886	96.6	E	Hot
7 <sub>0</sub> – 7 <sub>-1</sub>	156.82848	78.1	E	Hot
6 <sub>0</sub> – 6 <sub>-1</sub>	157.04859	61.8	E	Cold
5 <sub>0</sub> – 5 <sub>-1</sub>	157.17896	47.9	E	Cold
4 <sub>0</sub> – 4 <sub>-1</sub>	157.24604	36.3	E	Cold
Detected <sup>13</sup> CH <sub>3</sub> OH Lines				
8 <sub>0</sub> – 8 <sub>-1</sub>	155.69574	94.6	E	...
6 <sub>0</sub> – 6 <sub>-1</sub>	156.18652	60.7	E	...
5 <sub>0</sub> – 5 <sub>-1</sub>	156.29937	47.1	E	...
4 <sub>0</sub> – 4 <sub>-1</sub>	156.35640	35.8	E	...

#### Notes.

<sup>a</sup> The rotational energy is denoted  $J_K$ , where  $J$  and  $K$  indicate the rotational quantum number and its projection along the symmetry axis, respectively.

<sup>b</sup> Nuclear spin state of three hydrogens around the carbon (E: Ortho, A: Para).

<sup>c</sup> We made a stacking image only for the hot transitions (Figure 2(b)), avoiding foreground absorption via the blueshifted outflow lobe.

size is 700 au in radius and completely encloses the compact dusty structure. The CH<sub>3</sub>OH emission has significantly decreased toward the center, which is consistent with the optically thick dust emission. Almost all of the CH<sub>3</sub>OH emission is from beyond 250 au in radius. Figure 2(c) shows the position–velocity ( $PV$ ) diagram of the CH<sub>3</sub>OH emission along the north–south direction (Appendix B). The entire velocity structure is roughly symmetric against the systemic velocity of the natal cloud ( $\sim -4.5$  km s<sup>-1</sup>).

We detected both the rotational spin-up motion and infalling motion at the same time (e.g., Sakai et al. 2014; Beuther et al. 2017). These kinematic features could be basically reproduced by a simple model of the infalling rotating envelope, as in the case of low-mass protostars (Sakai et al. 2014; Oya et al. 2016). Figure 2(d) shows the schematic view of our model, which is described in Appendix B. The envelope is rotating counter-clockwise around the rotational axis that is inclined 8° from the LOS (Motogi et al. 2016, 2017). The envelope becomes thicker outward with a constant flaring angle. We adopted the specific angular momentum of  $2.4 \times 10^{21}$  cm<sup>2</sup> s<sup>-1</sup> in the model. This corresponds to the centrifugal radius of  $\sim 250$  au, which is consistent with the outer radius of the resolved structure in Figure 1(b) assuming the stellar mass of  $10 M_{\odot}$ .

We calculated the LOS velocities on the midplane and the near/far side of the envelope surface (Figure 2(d)). We have found that the envelope should have a relatively wide flaring angle ( $\sim 35^\circ$ ), in order to reproduce the rotational spin-up motion and the centrifugal brake against the infall acceleration. For example, if the envelope is geometrically thin with a much smaller flaring angle, the velocity field coincides with that in the midplane. On the other hand, the specific angular momentum that is significantly smaller than the assumed value could not reproduce the feature of the centrifugal braking. Conversely, the rotational spin-up feature at the angular offset of  $\pm 0.2$  could not be reproduced by the significantly larger angular momentum. Therefore, we suggest that the inner dust

emission traces a centrifugal disk and the rotating accretion flow reaches Keplerian rotation inside 250 au. It should be noted that further fine-tuned model fitting is beyond the scope of this study, because we clearly require higher spectral resolution and better sensitivity to detect any faint high-velocity emission.

We also detected four <sup>13</sup>CH<sub>3</sub>OH lines (Figure 2(a) and Table 2). The spatial structures of those <sup>13</sup>CH<sub>3</sub>OH lines are almost identical to that of the main isotopes. Surprisingly, the observed line ratio (CH<sub>3</sub>OH/<sup>13</sup>CH<sub>3</sub>OH) is very small ( $\sim 1.3$ ), suggesting that these line emissions are optically thick and almost thermalized. The averaged  $T_B$  of these optically thick CH<sub>3</sub>OH lines is  $\sim 100$  K. We used this value as the dust temperature in the outer envelope.

If we adopt the isotopic abundance ratio  $^{12}\text{C}/^{13}\text{C} \sim 60$ , the averaged optical depth of  $\sim 90$  is expected for the main isotopes. By using the non-local thermodynamic equilibrium radiative transfer code (RADEX: van der Tak et al. 2007), we estimated the lower-limit density ( $n_{\text{H}_2}$ ) and column density ( $N_{\text{CH}_3\text{OH}}$ ) as  $3 \times 10^9$  cm<sup>-3</sup> and  $10^{19}$  cm<sup>-2</sup>, respectively. Here, we adopted a kinematic temperature of 100 K and velocity dispersion of 5 km s<sup>-1</sup>, which is the observed line width (FWHM). The lower-limit  $N_{\text{H}_2}$  is  $\sim 10^{25}$  cm<sup>-2</sup>, assuming the relative CH<sub>3</sub>OH abundance of  $10^{-6}$ , which is the highest abundance observed in hot cores (e.g., Bisschop et al. 2007). We finally obtained a total envelope mass of  $7 M_{\odot}$  using the averaged radius of 700 au. This is comparable with that estimated from the dust emission ( $\sim 5 M_{\odot}$ ).

We note that actual dust temperature might be colder than the gas temperature estimated by line emission, because of different spatial locations in the disk/envelope as suggested in recent observational studies (e.g., Beuther et al. 2017). The envelope mass estimated by dust emission could be larger in this case.

### 3.3. Accretion Rate and Stellar Properties

The kinematic model indicates that an infalling timescale of the molecular envelope is  $\sim 10^3$  yr. This was estimated by numerically solving the equation of motion along the envelope surface for the mass particle at the outer edge. Here we only considered the stellar gravity and centrifugal force in the equation. On the other hand, the averaged envelope density of  $3.5 \times 10^{-15}$  g cm<sup>-3</sup>, where  $6 M_{\odot}$  is divided by the volume of the modeled envelope, corresponds the freefall time of  $\sim 1.1 \times 10^3$  yr. These are comparable, but the numerical value is slightly shorter than the freefall time because of the stellar gravity. The averaged infall rate inside the envelope is  $\sim 6 \times 10^{-3} M_{\odot} \text{ yr}^{-1}$ . We expect an effective accretion rate onto the stellar surface as  $3 \times 10^{-3} M_{\odot} \text{ yr}^{-1}$  or higher, because 50% of accreting mass could be converted to the outflow in case of high-mass star formation (e.g., Matsushita et al. 2017).

This infall rate is clearly larger than that estimated from the Jeans mass (i.e.,  $\sim c_s^3/G$ ). It becomes  $\sim 10^{-4} M_{\odot} \text{ yr}^{-1}$ , even adopting the current envelope temperature of 100 K. This discrepancy is usual in high-mass star formation, where we must consider the so-called effective Jeans mass, including a non-thermal velocity component such as turbulent or Alfvén velocities (e.g., Hosokawa & Omukai 2009; Inoue & Fukui 2013). We can replace  $c_s$  with  $c_{\text{eff}}$ , which is the root sum square of the velocity components in this case. The observed infall rate corresponds  $c_{\text{eff}}$  of  $\sim 3$  km s<sup>-1</sup>, suggesting a highly turbulent and/or strongly magnetized condition of the

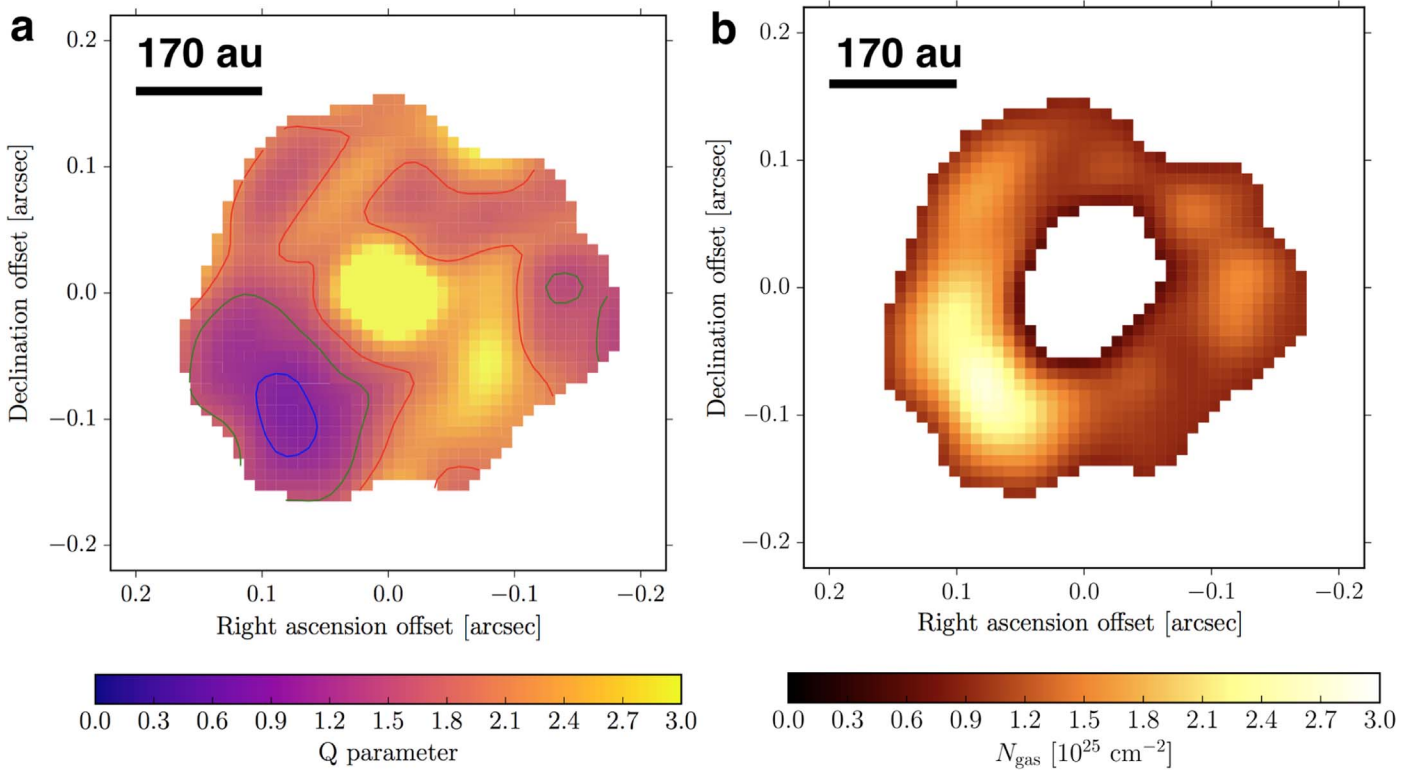


**Figure 3.** (a) Distribution of Toomre’s  $Q$  parameter. Blue, green, and red contours indicate  $Q = 1.0$ ,  $1.5$ , and  $2.0$ , respectively. The low brightness regions in Figure 1(b) ( $<40$  K) were masked and are shown in white. (b) Distribution of the surface density in the residual image. The minimum and maximum surface densities are 0.6 and 2.8, respectively. The low brightness regions ( $<40$  K) are also shown in white.

initial core. Such a condition may be achieved by dynamical compression via cloud–cloud collision (e.g., Inoue & Fukui 2013), rather than simple gravitational condensation.

The age of G353 could be only  $3 \times 10^3$  yr, considering the infall rate of  $3 \times 10^{-3} M_{\odot} \text{ yr}^{-1}$ . We note that the accretion rate onto the stellar surface from the disk can be highly variable in the case of the gravitationally unstable disk; however, the time-averaged accretion rate should be consistent with the infall rate onto the disk from the envelope (e.g., Meyer et al. 2018) after subtracting the outflow rate. We suggest that G353 is one of the youngest ( $<10^4$  yr) high-mass objects currently known, even considering an overall error of factor 3. The final stellar mass could be  $13\text{--}17 M_{\odot}$  depending on the outflow efficiency. It should be noted that this is still the lower-limit mass, as any envelope structure larger than  $0''.5$  should be resolved out in our data. Further observations on a larger scale are required to confirm the final stellar mass and its evolutionary stage.

### 3.4. Gravitational Stability of the Disk

The disk mass within 250 au reaches almost 20% of the stellar mass; therefore, the disk could be self-gravitating (Forgan et al. 2016). Figure 3(a) shows the spatial distribution of Toomre’s  $Q$  parameter (Toomre 1964; see Appendix C), which is a well-known measure of the gravitational stability ( $Q < 1$ : the disk immediately collapses;  $1 < Q < 2$ : the disk is unstable against non-axisymmetric perturbations). The central region shows  $Q > 2$ , suggesting that the disk is stabilized by the stellar radiation and stronger gravity of the central star. On the other hand, a significant fraction of the outer disk shows that  $Q < 2$  and the minimum  $Q$  reaches 0.9 around the eastern local peak. This fact indicates that the disk is, at least, unstable

against non-axisymmetric perturbations such as a spiral arm (e.g., Tomida et al. 2017). Furthermore, the averaged  $Q$  of  $\sim 1.9$  outside 80 au in radius suggests that the entire disk is moderately unstable, avoiding immediate collapse during the freefall time ( $\sim$ a few hundred yr). Such a short timescale is too short to be observed.

Although these criteria are valid for low-mass star formation, it may not be the case for high-mass star formation. Recent high-resolution numerical studies in Meyer et al. (2018) pointed out refined criteria ( $Q < 1$  for spiral arms,  $Q < 0.6$  for fragmentation). They also found that a disk-to-star mass ratio is 0.5 or higher in the case of the unstable disk. These new criteria suggest that our observed  $Q$  could be a little too high for the disks to be gravitationally unstable. The major uncertainty of  $Q$  in this study originates from the uncertainty of the dust opacity index  $\beta$ , which is used for estimating the surface density  $\Sigma$ . The uncertainty from errors in the sound velocity  $c_s$  and angular velocity  $\Omega$  is limited, because these are proportional to the square root of a temperature or stellar mass. We note that  $\beta$  could vary within 1–2, as discussed in Appendix A. Although we adopted  $\beta$  of unity for conservative mass estimation; if  $\beta = 2$  is adopted, the dust mass opacity  $\kappa_{\nu}$  becomes 40% smaller. The total disk mass reaches  $7 M_{\odot}$  within 250 au ( $5 M_{\odot}$  for the compact source within 100 au) in this case. We also obtain a 13% lower dust temperature, because higher optical depth is expected at the center (see Appendix A). This results in the averaged column density of  $5.3 \times 10^{26} \text{ cm}^{-2}$  for the compact source and  $2.4 \times 10^{25} \text{ cm}^{-2}$  for the resolved disk. Recalculated  $Q$  values are 0.9 (average), 0.4 (minimum), and 2.0 (maximum) in the resolved disk. This is more consistent with the results of Meyer et al. (2018).

The spatial scale of the simulated disk in Meyer et al. (2018) is quite similar to that of our observed disk, allowing us to directly compare disk structures. For example, we estimated the gas density of the disk, using the observed column density and disk scale height ( $H \sim c_s/\Omega$ ). We obtained  $H \sim 13$  au, at the radius of 100 au (see Appendix C for  $c_s$  and  $\Omega$  estimation). The gas density at 100 au is estimated as  $1.7 \times 10^{-12}$  g cm $^{-3}$  for  $\beta = 1$  and  $1.2 \times 10^{-11}$  g cm $^{-3}$  for  $\beta = 2$ . The latter value is comparable to that reported in Meyer et al. (2018). These comparisons could imply that  $\beta = 2$  is a more adequate choice for G353; this will be examined by ongoing follow-up multi-band ALMA observations.

Although  $\beta$  uncertainty remains, the disk in G353 is the most self-gravitating disk currently known. We propose that this is the first detection of a gravitationally unstable accretion disk in high-mass star formation. The obtained  $Q$  values are significantly smaller than those estimated in previous studies toward high-mass star-forming regions (Beuther et al. 2017; Ahmadi et al. 2018). This fact could be also explained by the young age of G353; i.e., the host object is still relatively less massive compared to other disk candidates, and the disk itself consists of gas with a smaller angular momentum at the inner region of the natal core. It is evident that radiative heating from the  $10 M_\odot$  accreting star is insufficient to stabilize the young massive disk with the radius of 250 au. The highly time-dependent outflow activity (Motogi et al. 2011, 2016) may be related to the unstable nature of the accretion flow.

The detected asymmetric structure can be also naturally explained by self-gravitating effects. The observed surface density contrast (up to 4–5; Figure 3(b)) is easily produced by a spiral arm. If this is the case, the gravitational torque can redistribute angular momentum in the disk. Such an effect can produce further infalling streams within the inner region (<100 au) found in the previous study (Motogi et al. 2017). The specific angular momentum of  $2.4 \times 10^{21}$  cm $^2$  s $^{-1}$  in the envelope is four times larger than that estimated for the inner streams. This indicates that 70% of the angular momentum is removed in the disk, probably via the gravitational torque. A rapid mass accretion to the central star promoted by non-axisymmetric structures decreases the disk surface density; therefore,  $Q$  should be adjusted to  $Q \sim 1$ –2 (e.g., Tomida et al. 2017) as seen in Figure 1(d).

Another possible origin of such asymmetric structures is a tidal perturbation via a close-encounter event by a nearby cluster member (e.g., Thies et al. 2010). However, this is unlikely to be the case because no bright cluster member was detected in the ALMA FOV. Our continuum sensitivity corresponds to a  $1\sigma$  dust mass sensitivity of  $8 \times 10^{-3} M_\odot$  beam $^{-1}$ , adopting a dust temperature of 100 K. It is clear that G353 is the first high-mass cluster member in the natal cluster-forming clump, although there may be a very small dust condensation that could form a brown dwarf.

The clumpy local peaks seen in the western region could also trace the fragmentation process in the disk. Indeed, the outer disk radius of  $\sim 250$  au and the minimum  $Q$  parameter of  $\sim 1$  are remarkably similar to that in the fragmented disk with the triplet low-mass protostar system in L1448 IRS3B (Tobin et al. 2016). These clumps may be the seed of a lower-mass binary companion, or accrete on the central object causing the accretion burst event (e.g., Meyer et al. 2017, 2018, 2019). The latter event was recently detected in several objects (Caratti o Garatti et al. 2017; Hunter et al. 2018). The masses of two large

clumps are 0.04 and 0.09  $M_\odot$  (Appendix D). These masses are for the  $\beta = 1$  case, and they are twice as large for the  $\beta = 2$  case.

For comparison, we estimated the Jeans scale ( $\lambda_J$ ) and Jeans mass ( $M_J$ ), in the disk. For the  $\beta = 1$  condition, the gas density is  $1.6 \times 10^{-13}$  g cm $^{-3}$  and the temperature is  $\sim 230$  K at 250 au radius. The former was estimated from the averaged surface density of  $1.0 \times 10^{25}$  cm $^{-2}$  in the eastern region, divided by the scale height of  $\sim 43$  au. We finally obtained  $\lambda_J$  of  $\sim 104$  au ( $0''.06$ ) and  $M_J$  of  $\sim 0.07 M_\odot$ . This is consistent with the observationally estimated masses of the clumps, and is still comparable even for the  $\beta = 2$  condition, where  $\lambda_J$  and  $M_J$  decrease by 40%. Although the estimated clump masses are 10–20 times larger than the accreting mass in the burst event in S255IR (Caratti o Garatti et al. 2017), it is consistent with the clump mass range formed by the disk fragmentation events in the numerical studies in Meyer et al. (2019).

Further high-resolution (< $0''.05$ ) ALMA observations are required in order to directly investigate the innermost region. In this case, it is possible that the dust emission could be completely optically thick in a higher frequency than ALMA band 4. Lower-frequency interferometers such as the Square Kilometer Array or Next Generation Very Large Array may be able to resolve the innermost accretion process.

#### 4. Conclusions

This study reports a new ALMA long baseline observation toward the nearly face-on accretion system around the high-mass protostellar object of  $10 M_\odot$ . We have successfully resolved the infalling rotating envelope ( $5$ – $7 M_\odot$ , 700 au in radius) and innermost centrifugal disk ( $2$ – $7 M_\odot$ , 250 au in radius). The estimated envelope accretion rate suggests that the target object can be well younger than  $10^4$  yr and still in the midpoint of its main accretion phase. The disk has typical Toomre’s  $Q$  parameters of 1–2 at 100–250 au radius. The minimum  $Q$  reaches 0.4 under the largest dust opacity index of 2. This suggests that the disk in G353 is highly self-gravitating and gravitationally unstable. The observed non-axisymmetric disk structures are consistent with this picture. We found that 70% of the initial angular momentum in the accretion flow could be removed via a gravitational effect such as a spiral arm. Our study suggests that the dynamical nature of a self-gravitating disk could dominate the early phase of high-mass star formation. This is remarkably consistent with the early evolutionary scenario of the low-mass protostar.

This first bird’s-eye view has also signaled the fact that the era of disk survey in high-mass star formation has ended; its detailed structure and diversities must be surveyed in the next decade. We emphasize that the viewing angle is critically important in order to study the innermost region of the massive disk. One must keep in mind the possibility that self-gravitating and unstable structure may exist, even in the cases of edge-on disks, apart from the stabilized and homogeneous Keplerian disk.

We thank A.J. Walsh and K. Tanaka for helpful comments and discussions in the observational strategy and analysis. We appreciate the anonymous referee’s fruitful comments and suggestions. This work makes use of the ALMA data set ADS/JAO.ALMA#2016.1.01068.S. ALMA is a partnership of ESO (representing its member states), NSF (USA) and NINS (Japan), together with NRC (Canada), MOST and ASIAA

(Taiwan), and KASI (Republic of Korea), in cooperation with the Republic of Chile. The Joint ALMA Observatory is operated by ESO, AUI/NRAO and NAOJ. This work was financially supported by the MEXT/JSPS KAKENHI grant No. 15K17613 and 19H05082 (K.M.). K.M. was also supported by the ALMA Japan Research Grant of NAOJ ALMA Project, NAOJ-ALMA-219. T.H. is financially supported by the MEXT/JSPS KAKENHI grant No. 16K05293, 17K05398, and 18H05222. S.T. acknowledges a grant from JSPS KAKENHI grant No. JP18K03703. This work was supported by NAOJ ALMA Scientific Research grant No. 2017-04A (S.T.).

*Software:* CASA (McMullin et al. 2007), PyFITS (Barrett & Bridgman 1999), Matplotlib (Hunter 2007).

*Facility:* ALMA.

## Appendix A Dust Continuum Emission

In order to highlight the resolved circumstellar structure, we performed the elliptical Gaussian fitting for the compact dust continuum emission, and then, the best-fit Gaussian was subtracted from the original image (Table 1). The effect of this subtraction is less than 20 K at the midpoint of the residual ring in Figure 1(b). This does not change any conclusions in this paper. The spectral index of the compact component was determined using the total fluxes in Table 1.

Most of the physical parameters of the dust continuum were estimated using the dust mass opacity at frequency  $\nu$  ( $\kappa_\nu$ ), dust opacity index  $\beta$  and the gas-to-dust ratio ( $R_{\text{gd}}$ ). In this paper, we adopted  $\kappa_\nu = 0.90 \times (\nu/230 \text{ GHz})^\beta \text{ cm}^2 \text{ g}^{-1}$ , where we assumed the dust model coagulated in the dense gas ( $10^6 \text{ cm}^{-3}$ ) with the thin ice mantle (Ossenkopf & Henning 1994). Unless the typical size of the dust particle is very large as in the evolved protoplanetary disks (Li et al. 2017),  $\beta$  usually lies between 1 and 2 (e.g., Tobin et al. 2016; Beuther et al. 2017). We adopted  $\beta = 1.0$  in this work, and hence,  $\kappa_{150 \text{ GHz}}$  is to be  $0.59 \text{ cm}^2 \text{ g}^{-1}$ . This is a conservative choice, i.e., higher  $\beta$  results in a more massive disk with lower  $Q$  value. It should be noted that  $\beta < 1.0$  may be possible if the compact emission is optically thin, where the spectral index  $\alpha$  is expressed as  $\alpha = 2 + \beta$ . This is, however, clearly not the case, considering the absence of the CH<sub>3</sub>OH lines toward the center.

The averaged optical depth ( $\tau_\nu$ ) and averaged dust temperature of the compact component ( $T_{\text{ave}}$ ) were determined by fitting the fluxes and source sizes at 45 and 150 GHz in Table 1. We used the Planck function and the relation  $\tau_{150 \text{ GHz}} = \tau_{45 \text{ GHz}} (150 \text{ GHz}/45 \text{ GHz})^\beta$  in the fitting. The estimated  $\tau_{150 \text{ GHz}}$  and  $T_{\text{ave}}$  are 2.0 and 555 K, respectively. We note that any contribution from a free-free emission is negligible ( $\sim 1$  mJy or less) as suggested by Motogi et al. (2017). Next, obtained  $\tau_{150 \text{ GHz}}$  was converted to the surface density of the dusty gas as,

$$\Sigma = \frac{\tau_\nu}{\kappa_\nu} R_{\text{gd}}.$$

The total mass was, then, acquired by integrating  $\Sigma$  over the source size.

On the other hand, physical parameters in the resolved structure were estimated by the following procedure. We first assumed the power-law profile of the dust temperature as,  $T_{\text{dust}}(r) = T_{80 \text{ au}}(r/80 \text{ au})^{-0.4}$  K, where  $r$  indicates a radius from the center. The referenced radius of 80 au is the averaged

radius of the compact dust component. The assumed power-law index of  $-0.4$  is a typical value for the embedded disk (e.g., Johnston et al. 2015). The referenced temperature  $T_{80 \text{ au}}$  was determined as 360 K, so as to match the averaged  $T_{\text{dust}}(r)$  inside 80 au and  $T_{\text{ave}}$ . We, then, calculated  $\tau_\nu$  from the ratio between  $T_{\text{dust}}$  and observed  $T_{\text{B}}$  in the resolved structure pixel-by-pixel as follows,

$$\tau_\nu = \ln \left( \frac{T_{\text{dust}}}{T_{\text{dust}} - T_{\text{B}}} \right).$$

Finally, the obtained spatial profile of  $\tau_\nu$  was converted to the surface density profile and total mass by using  $\kappa_{150 \text{ GHz}}$  and  $R_{\text{gd}}$  again. As mentioned in the main text, the dynamical heating effect by the non-axisymmetric disk structure can cause a deviation from the assumed  $T_{\text{dust}}(r)$  profile, i.e., spiral arms could have a higher temperature than surrounding region, because of gas compression. We clearly require further spatial resolution and/or multi-band data set for discussing such a detailed condition.

## Appendix B CH<sub>3</sub>OH Lines and Infalling Rotating Envelope

Since all the detected CH<sub>3</sub>OH lines showed similar spatial and kinematic profiles, we stacked multiple lines for better sensitivity. We divided detected lines into two categories based on the upper-state energy, i.e., “hot” transitions ( $>70$  K) and “cold” transitions ( $<70$  K). The stacking image and  $PV$  diagram were made only for hot transitions (Figure 2(b)), because the cold transitions showed a significant absorption feature in the blueshifted outflow lobe. This outflow absorption will be reported in the forthcoming paper. The final image noise level ( $1\sigma$ ) was  $1.1 \text{ mJy beam}^{-1}$  or 7.5 K. We adopted the cutoff signal-to-noise ratio of  $10\sigma$  ( $\pm 75$  K) for the integrated flux image. The regions outside this criterion were masked and shown by white color in Figure 2(b). The  $PV$  diagram (Figure 2(c)) was made along the R.A. offset  $=0''$ , from north to south.

We used the kinematic model of the infalling rotating envelope developed for the low-mass protostars (e.g., Sakai et al. 2014; Oya et al. 2016), which considers the conservation of energy and specific angular momentum. The rotational velocity ( $v_{\text{rot}}$ ) and infall velocity ( $v_{\text{inf}}$ ) are expressed as,

$$v_{\text{rot}} = \frac{l}{r_{\text{rot}}}$$

$$v_{\text{inf}} = \sqrt{\frac{2GM_{\text{in}}}{r} - \left( \frac{l}{r_{\text{rot}}} \right)^2},$$

where  $G$  is the gravitational constant and  $r_{\text{rot}}$  is the projection of the radius  $r$  to the envelope midplane.  $M_{\text{in}}$  is the enclosed mass that is fixed to  $12 M_\odot$  ( $10 M_\odot$  for the star and  $2 M_\odot$  for the inner dusty disk). The specific angular momentum  $l$  is also fixed to  $2.4 \times 10^{21} \text{ cm}^2 \text{ s}^{-1}$ , in order to have the centrifugal radius of 250 au that is the outer radius of the dusty disk. The rotational axis is set to be slightly inclined ( $8^\circ$ ) to due east from the LOS as suggested by previous studies (Motogi et al. 2016, 2017). We assume that the envelope is rotating counterclockwise and purely axisymmetric. The latter is adequate along the north-south direction, although the east-west asymmetry is clear in

Figure 2(b). The envelope becomes geometrically thicker outwards and the flaring angle is set to be constant for simplicity. We did not consider any outflow contribution in the north–south direction, since the compact water maser jet in similar spatial scale was clearly along the east–west direction (e.g., Motogi et al. 2016, 2017).

### Appendix C Toomre’s $Q$ Parameter

Toomre’s  $Q$  parameter is expressed as

$$Q = \frac{c_s \kappa}{\pi G \Sigma},$$

where  $c_s$  is the sound velocity,  $\kappa$  is the epicyclic frequency,  $\Sigma$  is the surface density. We calculated  $c_s$  from the  $T_{\text{dust}}(r)$ . The profile of  $\Sigma$  is already given by the analysis above.  $k$  is given by the angular velocity assuming that the dusty disk is in the Keplerian rotation around  $10 M_{\odot}$  star.

### Appendix D Clump Mass

We defined two large clumps in the west by the surface density above  $1.0 \times 10^{25} \text{ cm}^{-2}$  that is the average surface density in the western region. The clump masses were estimated to be 0.04 and  $0.09 M_{\odot}$ , integrating the surface densities.

### ORCID iDs

Tomoya Hirota  <https://orcid.org/0000-0003-1659-095X>  
 Masahiro N. Machida  <https://orcid.org/0000-0002-0963-0872>  
 Yoshinori Yonekura  <https://orcid.org/0000-0001-5615-5464>  
 Mareki Honma  <https://orcid.org/0000-0003-4058-9000>

### References

Ahmadi, A., Beuther, H., Mottram, J. C., et al. 2018, *A&A*, 618, A46

- Barrett, P. E., & Bridgman, W. T. 1999, *adass VIII*, 172, 483  
 Beltrán, M. T., & de Wit, W. J. 2016, *A&ARv*, 24, 6  
 Beuther, H., Walsh, A. J., Johnston, K. G., et al. 2017, *A&A*, 603, A10  
 Bisschop, S. E., Jørgensen, J. K., van Dishoeck, E. F., & de Wachter, E. B. M. 2007, *A&A*, 465, 913  
 Caratti o Garatti, A., Stecklum, B., Garcia Lopez, R., et al. 2017, *NatPh*, 13, 276  
 Cesaroni, R., Galli, D., Lodato, G., Walmsley, M., & Zhang, Q. 2006, *Natur*, 444, 703  
 Cesaroni, R., Galli, D., Neri, R., & Walmsley, C. M. 2014, *A&A*, 566, A73  
 Forgan, D. H., Ilee, J. D., Cyganowski, C. J., Brogan, C. L., & Hunter, T. R. 2016, *MNRAS*, 463, 957  
 Hirota, T., Machida, M. N., Matsushita, Y., et al. 2017, *NatAs*, 1, 0146  
 Hosokawa, T., & Omukai, K. 2009, *ApJ*, 691, 823  
 Hosokawa, T., Yorke, H. W., & Omukai, K. 2010, *ApJ*, 721, 478  
 Hunter, J. D. 2007, *CSE*, 9, 90  
 Hunter, T. R., Brogan, C. L., MacLeod, G. C., et al. 2018, *ApJ*, 854, 170  
 Inoue, T., & Fukui, Y. 2013, *ApJL*, 774, L31  
 Johnston, K. G., Robitaille, T. P., Beuther, H., et al. 2015, *ApJL*, 813, L19  
 Li, J. I., Liu, H. B., Hasegawa, Y., & Hirano, N. 2017, *ApJ*, 840, 72  
 Matsushita, Y., Machida, M. N., Sakurai, Y., & Hosokawa, T. 2017, *MNRAS*, 470, 1026  
 McMullin, J. P., Waters, B., Schiebel, D., Young, W., & Golap, K. 2007, *adass XVI*, 376, 127  
 Meyer, D. M.-A., Kuiper, R., Kley, W., Johnston, K. G., & Vorobyov, E. 2018, *MNRAS*, 473, 3615  
 Meyer, D. M.-A., Vorobyov, E. I., Elbakyan, V. G., et al. 2019, *MNRAS*, 482, 5459  
 Meyer, D. M.-A., Vorobyov, E. I., Kuiper, R., & Kley, W. 2017, *MNRAS*, 464, L90  
 Motogi, K., Hirota, T., Sorai, K., et al. 2017, *ApJ*, 849, 23  
 Motogi, K., Sorai, K., Honma, M., et al. 2011, *MNRAS*, 417, 238  
 Motogi, K., Sorai, K., Honma, M., et al. 2016, *PASJ*, 68, 69  
 Motogi, K., Sorai, K., Niinuma, K., et al. 2013, *MNRAS*, 428, 349  
 Ossenkopf, V., & Henning, T. 1994, *A&A*, 291, 943  
 Oya, Y., Sakai, N., López-Sepulcre, A., et al. 2016, *ApJ*, 824, 88  
 Sakai, N., Sakai, T., Hirota, T., et al. 2014, *Natur*, 507, 78  
 Thies, I., Kroupa, P., Goodwin, S. P., Stamatellos, D., & Whitworth, A. P. 2010, *ApJ*, 717, 577  
 Tobin, J. J., Kratter, K. M., Persson, M. V., et al. 2016, *Natur*, 538, 483  
 Tomida, K., Machida, M. N., Hosokawa, T., Sakurai, Y., & Lin, C. H. 2017, *ApJL*, 835, L11  
 Toomre, A. 1964, *ApJ*, 139, 1217  
 van der Tak, F. F. S., Black, J. H., Schöier, F. L., Jansen, D. J., & van Dishoeck, E. F. 2007, *A&A*, 468, 627